

Article

# Investigation of Stray Radiation Suppression in Infrared Imaging System Using a Novel Broadband and High-Absorption Ceramic Coating

Zhen Yang<sup>1,2,3</sup>, Xinmin Guo<sup>1,2,\*</sup>, Songtao Lu<sup>4</sup>, Yong Zhang<sup>1,2</sup>, Haili Hu<sup>1,2</sup>, Kaichang Lu<sup>1,2</sup> and Jianlong Zhang<sup>1,2,\*</sup>

<sup>1</sup> National Key Laboratory of Science and Technology on Tunable Laser, Harbin Institute of Technology, Harbin 150080, China; sailoryz@163.com (Z.Y.); zzyyyy@hit.edu.cn (Y.Z.); huhaili\_hit@163.com (H.H.); kaichanglu@hotmail.co.uk (K.L.)

<sup>2</sup> Department of Optoelectronic Information Science and Technology, Harbin Institute of Technology, Harbin 150001, China

<sup>3</sup> Post-Doctoral Mobile Station of Instrumentation Science and Technology, School of Instrumentation Science and Engineering, Harbin Institute of Technology, Harbin 150001, China

<sup>4</sup> School of Chemistry and Chemical Engineering, Harbin Institute of Technology, Harbin 150001, China; lusongtao@hit.edu.cn

\* Correspondence: guoxm@hit.edu.cn (X.G.); jianlongz@hit.edu.cn (J.Z.); Tel.: +86-0451-8640-3815 (X.G.)



**Citation:** Yang, Z.; Guo, X.; Lu, S.; Zhang, Y.; Hu, H.; Lu, K.; Zhang, J. Investigation of Stray Radiation Suppression in Infrared Imaging System Using a Novel Broadband and High-Absorption Ceramic Coating. *Appl. Sci.* **2021**, *11*, 4952. <https://doi.org/10.3390/app11114952>

Academic Editors: Yufei Ma, Yong Zhao and Bernhard Wilhelm Roth

Received: 26 April 2021  
Accepted: 26 May 2021  
Published: 27 May 2021

**Publisher's Note:** MDPI stays neutral with regard to jurisdictional claims in published maps and institutional affiliations.



**Copyright:** © 2021 by the authors. Licensee MDPI, Basel, Switzerland. This article is an open access article distributed under the terms and conditions of the Creative Commons Attribution (CC BY) license (<https://creativecommons.org/licenses/by/4.0/>).

**Abstract:** Aiming at addressing the vulnerability of the infrared imaging opto-mechanical system to stray radiation interference caused by an external laser, a new method with a broadband and high-absorptivity ceramic coating on the inner wall of the system is proposed to reduce the stray radiation intensity, which is helpful to improve the imaging quality of the detection image. Based on plasma electrolytic oxidation (PEO) technology, the preparation method and properties of a novel ceramic coating are studied, and a long-wave infrared imaging optical system with high-absorption ceramic coating is designed and developed. It is verified for the first time that the high-absorption ceramic coating can suppress the stray radiation in the infrared opto-mechanical system, and the effect of laser incident power and angle on the stray radiation is investigated. The experimental results show that the ceramic coating can achieve 95.4% high absorption in the wavelength range of 0.2–16  $\mu\text{m}$ , which can obviously suppress the stray radiation in the opto-mechanical system of infrared imaging caused by laser. The calculation of the stray radiation suppression ratio shows that, compared with the case without coating, the stray radiation intensity in the system can be reduced by 70% using the ceramic coating.

**Keywords:** stray radiation suppression; infrared imaging system; high-absorption ceramic coating; PEO

## 1. Introduction

In recent years, the rapid development of high-energy laser technology has posed a serious laser threat to traditional infrared imaging systems and high-sensitivity infrared detectors [1–5]. Laser damage to infrared imaging and detection systems can be divided into soft damage and hard damage. For soft damage, the lens or detector in the infrared photoelectric detection system is irradiated by laser with low power density, leading to a short-term functional failure. Hard damage usually involves the use of a laser with a high power density (up to several kW or tens of kW) to directly irradiate the target, which causes permanent damage. When the laser irradiation angle is close to the optical axis direction, that is, when the laser incidence angle is within the field-of-view (FOV) angle of the infrared imaging system, the laser directly damages the image plane of the detector, resulting in failure of the detection system. When the laser irradiates the components of the infrared imaging opto-mechanical system at a certain incident angle outside the FOV, such as the infrared optical lens, frame, or barrel, the laser forms a high-intensity scattering

light source in each irradiation area, resulting in different degrees of stray radiation at the image plane of the infrared detector. After multiple refraction and scattering, the stray light seriously affects the imaging quality and resolution of the infrared detection system. Therefore, the analysis and suppression of infrared stray radiation is very important to achieve high-precision infrared imaging detection.

In order to quantitatively study the distribution of stray radiation, the simulation method is widely used to analyze the stray radiation in optical imaging systems [6–10]. Although there are many simulation methods to effectively predict and analyze the stray light of infrared imaging optical systems, the causes of stray radiation are very complex, which are related not only to the design, manufacturing process, and material characteristics of the infrared imaging system, but also to the aberration, target surface characteristics, and thermal radiation of system components. The analysis of stray radiation from the perspective of simulation often leads to some defects and differences between the actual infrared imaging system and the design model. Therefore, the actual measurement is also an essential link and an important reference for the evaluation of stray radiation in the infrared imaging system.

According to the transmission theory of stray radiation, the basic methods for suppressing stray radiation are mainly divided into two kinds [11–13]: one involves controlling the direction of stray radiation energy transmission, which is realized by changing the path of light transmission, commonly by designing the physical structure of the lens and the shape of the light blocking ring to change the direction of beam transmission; the other involves achieving the attenuation of radiation energy by increasing the scattering times of stray radiation. In the actual production and processing process, the specific stray radiation suppression measures can be divided into three parts [14,15]: one involves optimizing the macrostructure of the infrared detection system, such as the lens hood and light blocking ring; the second involves improving the microstructure of the infrared detection system, such as increasing the roughness of the reflection surface; the third involves changing the optical characteristics of each inner surface in the infrared opto-mechanical system, such as coating and blackening treatment. The first two methods have been widely used to suppress the stray radiation in infrared imaging and detection systems. However, it is rare to apply an effective anti-stray radiation coating inside the infrared opto-mechanical system. Blackening is a common method. However, it is difficult to achieve high-absorptivity stray radiation absorption in a wide band; thus, the actual effect of eliminating stray radiation is rather limited. In this paper, a novel broadband and high-absorption nano ceramic coating is proposed to be coated on the inner wall of the infrared opto-mechanical system. By using the absorption characteristics of ceramic coating materials, the infrared stray radiation can be effectively absorbed, which can overcome the shortcomings of conventional blackening treatment in the long-wave infrared absorption rate and the narrow absorption spectrum range.

Ceramic materials have excellent oxidation resistance, corrosion resistance, high-temperature mechanical properties, and stability [16–18]. They allow for the creation of laser protective coatings with good comprehensive performance and excellent laser damage resistance. Generally, the preparation methods of ceramic coatings mainly include resin coating [19–21], air spraying [22–24], plasma spraying [25–27], and plasma electrolytic oxidation (PEO) [28–30]. Because the applied voltage in the PEO reaction breaks through the limitation of anodic oxidation in the Faraday region, under the action of high temperature and high pressure of micro plasma discharge, the surface of the substrate is melted and sintered, and then a typical porous ceramic oxide film is grown in situ. Research has shown that the bonding mode between the ceramic film and the substrate is typical metallurgical bonding, which can endow the matrix material with excellent mechanical and functional properties that cannot be achieved by other technologies. Therefore, compared with other conventional surface engineering technologies, PEO technology has many advantages, such as high hardness and electrical insulation, strong operability, close and firm combination with the substrate, relative simple preparation process, high processing speed,

unlimited requirements on the shape and size of the substrate, high cost performance, and suitability for automatic manufacturing and production [31–34]. However, the in situ growth process of a PEO ceramic coating is very complex, involving many aspects such as thermal diffusion, electrochemistry, and plasma technology. The laser damage resistance of the coating depends greatly on its chemical composition and structure size. Therefore, the preparation of ceramic coatings with high absorptivity, a wide spectral absorption range, and high adhesion requires several experiments and technical accumulation.

In this paper, we first studied the preparation method and material properties of a novel broadband ceramic coating with high absorption. Then, we coated the high-absorption ceramic coating on the aluminum alloy metal substrate and developed a long-wave infrared imaging optical system with the high-absorption ceramic coating on the inner wall. According to the above research results, the suppression effect of the high-absorption ceramic coating on the stray radiation formed by multiple scattering inside the infrared opto-mechanical system was investigated under different incident angles and different incident laser energy outside the FOV. The suppression ability of the coating on the long-wave infrared stray radiation was verified. Due to the low cost and small thickness of the ceramic coating used in this paper, the weight and structure of the infrared imaging system would not be changed much. Therefore, it is expected to be more widely used in the current system.

## 2. Transmission Model of Stray Radiation

Usually, due to the diversity of stray radiation sources and system design, it is difficult to obtain accurate mathematical expressions of stray radiation using theoretical methods. It is generally considered that stray radiation is transmitted from the previous stray radiation source to the next stray radiation source. The propagation process follows the law of energy conservation and satisfies the general law of light radiation propagation.

Figure 1 shows the radiation transmission between two micro-facets. According to the theory of radiative energy transmission, it is assumed that there are two Lambert micro surface elements  $dA_s$  and  $dA_r$ ; the distance between them is  $l$  and the radiance is  $L_s$  and  $L_r$ , respectively. The angles between the normal of the two facets and  $l$  are  $\theta_s$  and  $\theta_r$ , respectively. According to the definition of radiance, the radiation power emitted from  $dA_s$  to  $dA_r$  is as follows:

$$dP_{s \rightarrow r} = L_s \cos \theta_s dA_s d\Omega_{r \rightarrow s}, \quad (1)$$

where the solid angle of  $dA_r$  to  $dA_s$  can be expressed as follows:

$$d\Omega_{sr} = \frac{dA_s \cos \theta_s}{l^2}. \quad (2)$$

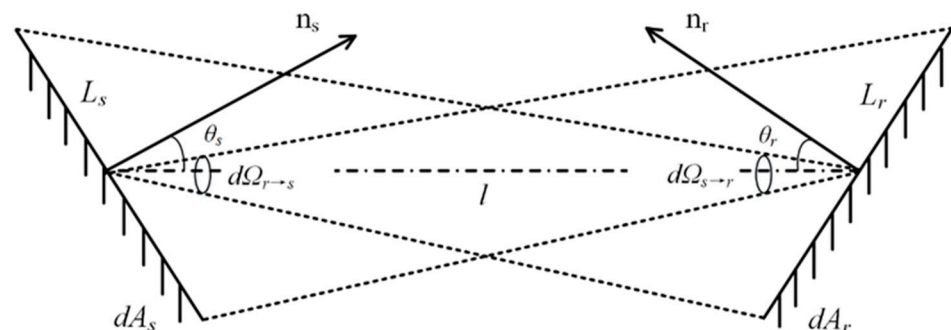


Figure 1. Schematic diagram of radiation transmission between two micro-facets.

By substituting Equation (2) into Equation (1), one can get

$$dP_{s \rightarrow r} = \frac{L_s \cos \theta_s \cos \theta_r dA_s dA_r}{l^2}. \quad (3)$$

It is assumed that the radiation energy incident on the micro-facet  $dA_s$  is  $d\Phi_s$ , and the energy reflected on the other surface is  $d\Phi_r$ . According to the definition of bidirectional reflectance distribution function (BRDF) for the Lambert radiation surface, the  $BRDF_s$  of the micro-facet  $dA_s$  can be expressed as follows:

$$BRDF_s = \frac{L_s}{E_s}, \quad (4)$$

where  $E_s$  is the irradiance on the micro-facet  $dA_s$ . By substituting Equation (4) into Equation (3), one can get

$$dP_{s \rightarrow r} = BRDF_s \cdot E_s \cdot \cos \theta_s \cdot dA_s \frac{dA_r \cdot \cos \theta_r}{l^2}. \quad (5)$$

The angular coefficient, also known as the shape factor, represents the geometric relationship between the source object and the receiving object. According to the definition, the angle coefficient  $dF_{s \rightarrow r}$  from micro-facet  $dA_s$  to  $dA_r$  can be described by the following expression:

$$dF_{s \rightarrow r} = \frac{dP_{s \rightarrow r}}{M_s dA_s} = \frac{\cos \theta_s \cos \theta_r}{\pi l^2} \cdot dA_r, \quad (6)$$

where the  $M_s$  is the radiant emittance of  $dA_s$ . The physical meaning of angular coefficient  $dF_{s \rightarrow r}$  is the ratio of the radiant power emitting from surface  $dA_s$  and received by surface  $dA_r$  to the total radiant power emitted from the surface.

Considering

$$d\Phi_s = E_s \cdot dA_s, \quad (7)$$

$$d\Phi_r = dP_{s \rightarrow r}, \quad (8)$$

one can get the following result by substituting Equations (6)–(8) into Equation (5):

$$d\Phi_r = d\Phi_s \cdot BRDF_s \cdot dF_{s \rightarrow r} \cdot \pi. \quad (9)$$

For the two finite surfaces, the result is as follows:

$$\Phi_r = \Phi_s \cdot BRDF_s \cdot F_{s \rightarrow r} \cdot \pi. \quad (10)$$

It can be seen from Equation (10) that the energy on the receiving surface is the product of three factors: the radiation power from the source surface, the BRDF of the source surface, and the angle coefficient  $F_{s \rightarrow r}$  from the source surface to the receiving surface. Therefore, in order to suppress the stray radiation in the infrared imaging system, the following methods are usually used: reducing the angle coefficient and the radiation power from the source surface as far as possible, and using the material with as low a BRDF as possible. There have been many studies on reducing the angle coefficient and the source surface emission power, but there are no reports on using a high-absorptivity ceramic coating to increase the absorption for stray radiation on the material surface, thereby reducing the BRDF. Therefore, in this paper, a novel high-absorption ceramic coating is applied on the inner surface of the infrared opto-mechanical system to reduce the surface reflectance of BRDF, so as to suppress the stray radiation from the outside of the FOV.

### 3. Preparation and Characteristics of High-Absorption Ceramic Coating

The broadband and high-absorptivity ceramic coating materials were prepared by liquid phase plasma electrolytic oxidation technology (LPPEO). LPPEO is a new type of surface coating preparation technology [35]. The basic principle is that the anode parts of valve metals or their alloys such as aluminum, magnesium, titanium, and zirconium are placed in a specific electrolyte system. By adjusting the external power supply, the spark discharge occurs on the anode surface. Under the action of instantaneous high tempera-

ture and high pressure in the micro area, the thermal diffusion and electric discharge are excited and enhanced on the anode surface. As a result, the oxide ceramic coating firmly bonded with the substrate is grown on the anode surface in situ. The surface absorption performance of ceramic coating is directly related to coating thickness, surface roughness, material microstructure, and composition. Previous studies have shown that these parameters are mainly affected by the power mode, electrolyte composition, power parameters, and oxidation time of PEO technology [36–38]. Therefore, the above factors affecting the surface absorption properties of ceramic coatings were investigated in this paper.

Firstly, the preparation process of the ceramic coating on the aluminum alloy substrate was studied from the design of a high-absorption ceramic coating and the selection of an electrolyte system. The ceramic coating with high absorptivity was prepared by using silicate and phosphate as main salts, zinc sulfate as a coloring salt, and sodium hydroxide. Then, the concentration of electrolyte composition was optimized by orthogonal test. Taking the infrared absorption rate of the coating as the performance parameter, the influence of electrolyte component concentration on the absorption rate of the coating was analyzed to optimize the concentration of each component in electrolyte. The experimental results show that the main factors affecting the absorption rate were the concentrations of  $\text{ZnSO}_4$  and  $\text{NaOH}$ , followed by silicate and phosphate.

Secondly, the effects of current density, power frequency, power duty cycle, and oxidation time on the surface absorption properties of ceramic coatings were studied. The results show that, when the current density was  $3.75 \text{ A/dm}^2$ , the frequency was 200 Hz, the duty cycle was 20%, and the oxidation time was 20 min, the coating thickness and surface roughness met the performance requirements. At the same time, the absorption rate of ceramic coating on aluminum alloy was highest. The average absorption rate of the ceramic coating was 95.4% in the range of 0.2–16  $\mu\text{m}$ . The ceramic coating samples on aluminum alloy substrate were prepared under the above conditions. The macrostructure, 350 $\times$  microstructure, and 1000 $\times$  microstructure features on the ceramic coating surface were observed using a charge coupled device (CCD) camera, optical microscope, and scanning electron microscope (SEM), respectively. The results are shown in Figure 2. The surface absorptivities of the ceramic coating and the aluminum alloy without coating in the visible and infrared bands (0.2–16  $\mu\text{m}$ ) were measured using an absorptivity tester, and the measurement results are shown in Figure 3. It can be seen from Figure 2 that the surface of the high-absorption ceramic coating presented a very dense porous structure. It could absorb a wide range of absorption from visible to long-wave infrared light, mainly because the radiation in different wavelengths would be absorbed by a large number of micro holes on the surface of the coating, and the photons entering the holes would transfer the energy to the coating material, thus achieving a broad absorption band and high absorptivity of photon energy.

Lastly, the average surface thickness and surface roughness of the coating under the optimal experimental parameters were obtained using a coating thickness meter and atomic force microscope (AFM). The average surface thickness and the average surface roughness of the coating were 43.9  $\mu\text{m}$  and 47.5 nm, respectively. The typical measurement results of surface roughness for ceramic coating are shown in Figure 4.

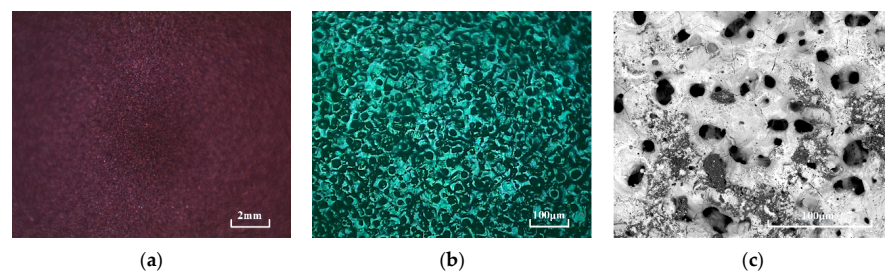


**Figure 2.** Macro and micro morphology characteristics of ceramic coating surface: (a) macro morphology; (b) 350 $\times$  optical micrograph; (c) 1000 $\times$  scanning electron microscope (SEM) micro morphology.

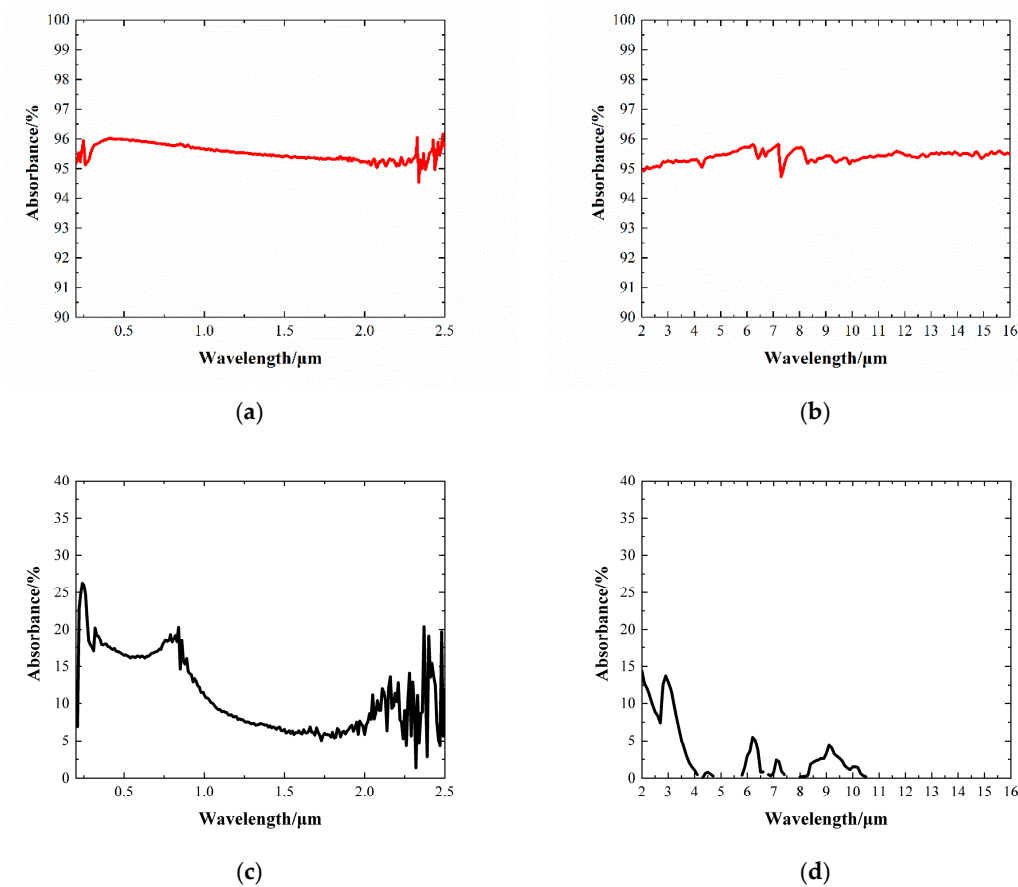


**Figure 3.** Measurement results of surface absorptivity for the ceramic coating and the aluminum alloy without coating in the range of visible to infrared light: (a) ceramic coating at  $\lambda = 0.2\text{--}2.5 \mu\text{m}$ ; (b) ceramic coating at  $\lambda = 2.0\text{--}16 \mu\text{m}$ ; (c) aluminum alloy without coating at  $\lambda = 0.2\text{--}2.5 \mu\text{m}$ ; (d) aluminum alloy without coating at  $\lambda = 2.0\text{--}16 \mu\text{m}$ .

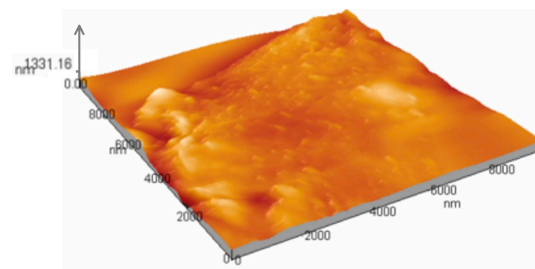


**Figure 4.** The atomic force microscope (AFM) measurement image of the ceramic coating surface.

#### 4. Experimental Setup

The stray radiation experimental measurement setup of the infrared imaging system based on the high-absorption ceramic coating is shown in Figure 5. The system mainly consisted of a  $\text{CO}_2$  laser at  $10.6 \mu\text{m}$ , laser beam expanding collimator, beam expander, infrared imaging opto-mechanical system and detector, DC power supply, laser power monitoring system, and constant-temperature heat source. In the experiment, the  $10.6 \mu\text{m}$  laser emitted by the  $\text{CO}_2$  laser was output through the beam expanding and collimating optics. The collimated laser first split 1/10 of the laser energy by the beam splitter, so as to monitor the laser power in real time; the remaining laser was reflected into the infrared beam expanding optics by the reflector. Then, the expanded laser entered the infrared imaging system. Because the laser was incident at a certain angle outside the FOV, the laser entering the infrared opto-mechanical system scattered several times in the inner wall of the system and then reached the image plane of the detector. The stray radiation image collected was transmitted to the data processing center. The constant-temperature

heat source was placed in the FOV of the infrared imaging opto-mechanical system, which was used as a reference target of the experiment. In this experimental system,  $\alpha$  is the incident angle when the expanding beam irradiates the infrared imaging system, and  $\theta$  is the angle of FOV for the infrared imaging system. The main parameters of the CO<sub>2</sub> laser, infrared imaging system, and uncooled detector used in the experimental system are shown in Table 1.

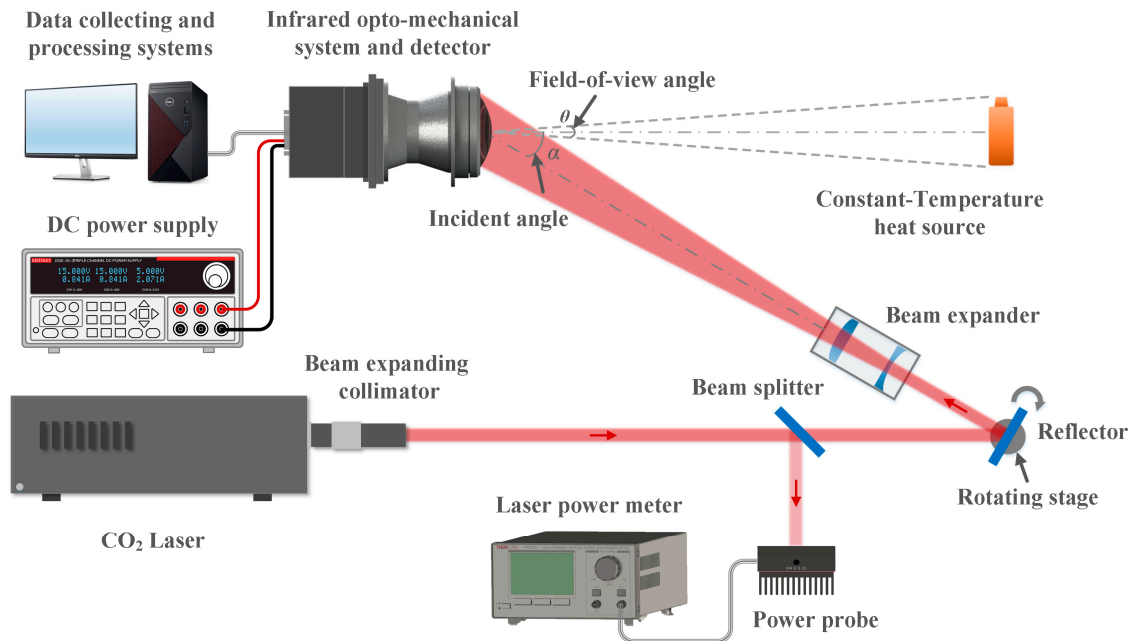
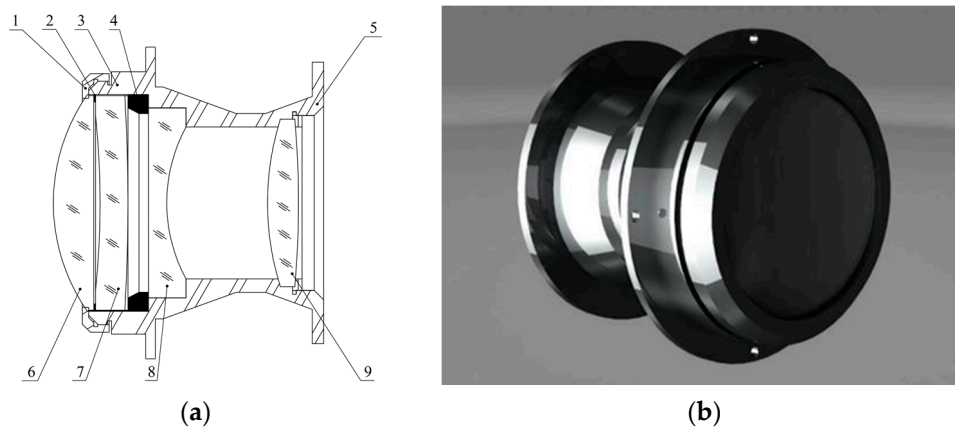


Figure 5. The stray radiation experimental setup of the infrared imaging system.

The design drawing and the three-dimensional schematic diagram of the infrared imaging opto-mechanical system are shown in Figure 6. The opto-mechanical system was made of aluminum alloy. In order to verify the absorption efficiency of stray radiation for the high-absorption ceramic coating, the LPPEO technology, combined with the forced convection technology for the coating uniformity control, was used to coat the ceramic coating on the inner wall of the infrared opto-mechanical system. The infrared opto-mechanical systems with and without ceramic coating were processed. The photographs of the system structure are shown in Figure 7.

Table 1. Main parameters of stray radiation experimental measurement system.

System Component	Parameter	Specifics
CO <sub>2</sub> laser	Maximum output power	1 W
	Wavelength	10.6 μm
	Power stability	±5%
Infrared imaging Optical system	Working wavelength	8~12 μm
	Exit pupil diameter	44 mm
	Entrance pupil diameter	57 mm
	Minimum resolvable temperature difference (MRTD)	450 mK (2.5 cycle/mrad)
Infrared detector	Resolution	640 × 512
	Pixel Size	17 μm
	f-Number	1
	Field-of-view (FOV) angle	10°



**Figure 6.** The design drawing and the three-dimensional schematic diagram of infrared imaging opto-mechanical system: (a) design drawing; 1: first lens pressing ring; 2: second lens spacer; 3: lens barrel; 4: third lens spacer; 5: fourth lens pressing ring; 6: first lens; 7: second lens; 8: third lens; 9: fourth lens; (b) three-dimensional schematic diagram.



**Figure 7.** Photographs of the infrared imaging opto-mechanical system: (a) without ceramic coating; (b) with ceramic coating.

Because of the noncomplete avoided background radiation, 10 background noise images were collected and averaged as the background noise images before the experiment. During the experiment, another 10 images were collected and averaged as stray radiation images with background noise. After the experiment, the collected data were processed. The specific method involved obtaining the grayscale difference matrix of the image by subtracting the background noise from the gray image with stray radiation. The image was the grayscale distribution image of the stray radiation after deducting the background noise.

## 5. Experimental Results and Discussion

### 5.1. Effect of Incident Power on Stray Radiation

It can be seen from Equation (10) that the stray radiation intensity received by the detector image plane was related to the laser incident power. The actual situation would be more complicated, because the stray radiation intensity reaching the detector image plane is affected by many factors, such as the stray light incident angle and internal geometry of opto-mechanical system. The ceramic coating also had a saturation absorption effect. In order to verify whether the high-absorption ceramic coating proposed in this paper can suppress the stray radiation and the variation of the suppression effect with the laser power and the laser incident angle, the effects of different incident conditions on the intensity of stray radiation in the infrared opto-mechanical system with a ceramic coating on the aluminum alloy substrate were investigated experimentally. In the experiment, the optical axis of the infrared optical imaging system was adjusted to the angle of  $50^\circ$  with the laser propagation direction. Then, the laser incident power was gradually increased from 0.1 W to 0.8 W. Lastly, the stray radiation distribution image on the image plane of the infrared

imaging detector was collected. The experimental results are shown in Figure 8. In order to compare and analyze the stray radiation images induced by lasers with different incident power, all images were normalized.

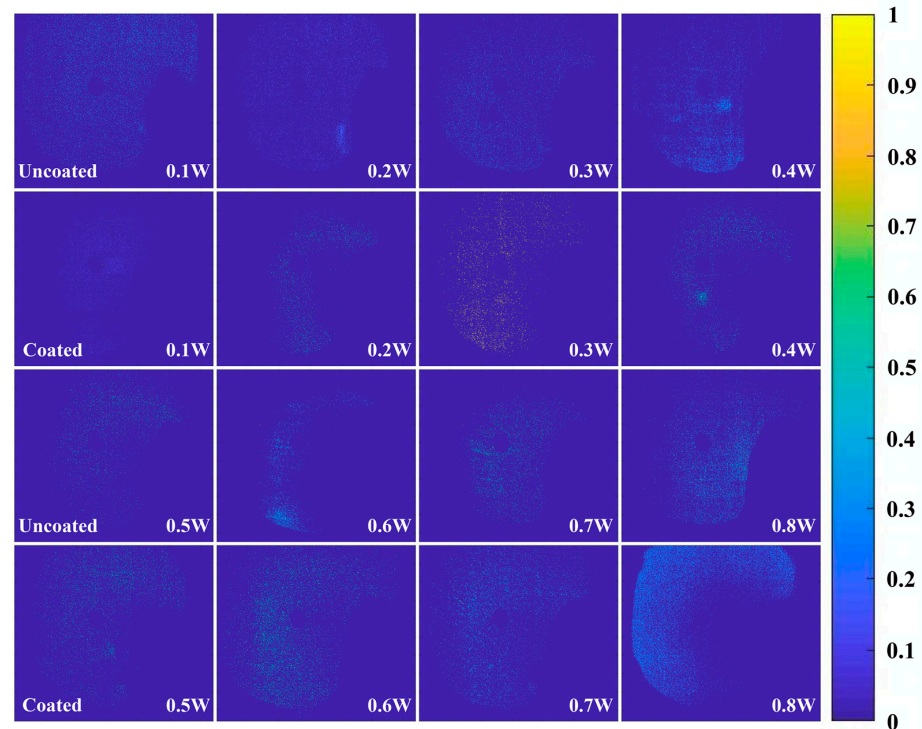


**Figure 8.** Variation of stray light distribution with laser incident power in optical mechanical system ( $\alpha = 50^\circ$ ).

As can be seen from Figure 8, the stray radiation distribution image mostly presented the shape of circular distribution. This is because the section of the inner wall of the lens was round and, therefore, the stray radiation into the opto-mechanical system was consistent with the geometry of the inner wall of the lens barrel. This experimental phenomenon could prove that the experimental results were indeed stray radiation images formed by multiple scattering from the inner wall in the opto-mechanical system. However, the two-dimensional spatial distribution of stray radiation intensity showed some randomness under different laser incident power, angle, and initial boundary conditions. The reason is that the spatial distribution of the spot energy for the initial incident laser in the experiment was different, and the surface roughness on the inner wall of the opto-mechanical system with and without coating was inconsistent, resulting in the different transmission paths of the stray radiation in the system. Therefore, the two-dimensional spatial distribution of the stray radiation intensity finally reaching the image plane of the detector was also different. Lastly, the stray light distribution on the image plane of the detector was randomly distributed.

In order to describe the variation of stray light intensity with laser incident power more clearly, we counted the number of stray radiation points in each measurement result. The specific statistical methods were as follows:

$$I_{\text{total}} = \frac{1}{N} \sum_k^l \sum_i^m \sum_j^n I^k(i, j) \quad (k = 1, \dots, l; i = 1, \dots, m; j = 1, \dots, n), \quad (11)$$

where the  $I_{\text{total}}$  represents the overall average stray radiation relative intensity of 10 collected stray radiation images,  $m$  and  $n$  represent the number of image rows and columns respectively ( $m = 480$  and  $n = 640$ ),  $N$  is the number of collected images ( $N = 10$ ),  $k$  is the serial number of collected images,  $i$  represents the  $i$ -th row of the  $k$ -th image, and  $j$

represents the  $j$ -th column of the  $k$ -th image. A higher value of  $I_{total}$  denotes stronger stray radiation. In this way, the overall average relative intensity of stray radiation could be used to quantitatively characterize the suppression degree of the stray radiation for the ceramic coating on the infrared opto-mechanical system and the variation with the incident laser power.

The variation of relative intensity for stray radiation in the opto-mechanical system with and without ceramic coating with laser incident power is shown in Figure 9. It can be seen that, for the aluminum alloy substrate material, when the incident laser power was less than 0.4 W, the stray radiation intensity with ceramic coating was generally weaker than the case without ceramic coating. However, when the incident laser power increased to 0.5–0.8 W, the stray radiation intensity with ceramic coating was stronger than that without ceramic coating. Because the surface of the ceramic coating prepared in this paper was composed of many small holes and had a high-absorption characteristic in a wide range of wavelengths, the principle underlying its absorption light energy is the spread of photons in the holes and transfer of energy to the ceramic material upon their entry into these small holes, before completely releasing the light energy carried. The number of holes on the surface of the ceramic coating was constant; therefore, the ceramic coating had a certain saturation absorption threshold. When the external radiation energy exceeded this threshold, the ceramic coating could not further absorb the remaining photon energy. Therefore, when the laser power was greater than 0.4 W, the ceramic coating reached the absorption saturation state and a large amount of remaining stray radiation directly reached the image plane of the detector, resulting in a rapid increase in the stray radiation intensity.

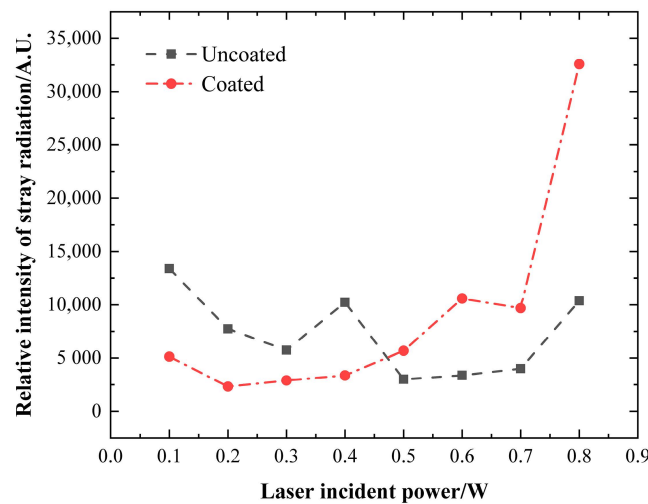


Figure 9. Variation of average stray radiation intensity with laser incident power ( $\alpha = 50^\circ$ ).

In order to further investigate the suppression degree of stray light after adding the ceramic coating, the average relative stray radiation suppression ratio  $R_{rel}$  was defined as

$$R_{rel} = \frac{\sum_i^m \sum_j^n I_0(i, j) - \sum_i^m \sum_j^n I_c(i, j)}{\sum_i^m \sum_j^n I_0(i, j)} \tag{12}$$

where  $I_0(i, j)$  represents the grayscale of the  $i$ -th row and  $j$ -th column in the stray radiation image without ceramic coating, while  $I_c(i, j)$  represents the grayscale of the  $i$ -th row and  $j$ -th column in the stray radiation image with ceramic coating. The average relative stray radiation suppression ratio  $R_{rel}$  reflects the stray radiation suppression ability of the ceramic coating. A higher  $R_{rel}$  denotes a higher stray radiation suppression ability of the ceramic coating. If  $R_{rel}$  is positive, it means that the ceramic coating has the ability to suppress stray radiation. If the value is negative, it means that adding the ceramic coating would increase

the stray radiation intensity. According to the definition of  $R_{rel}$ , the variation of  $R_{rel}$  for the ceramic coating with laser incident power was calculated, as shown in Figure 10.

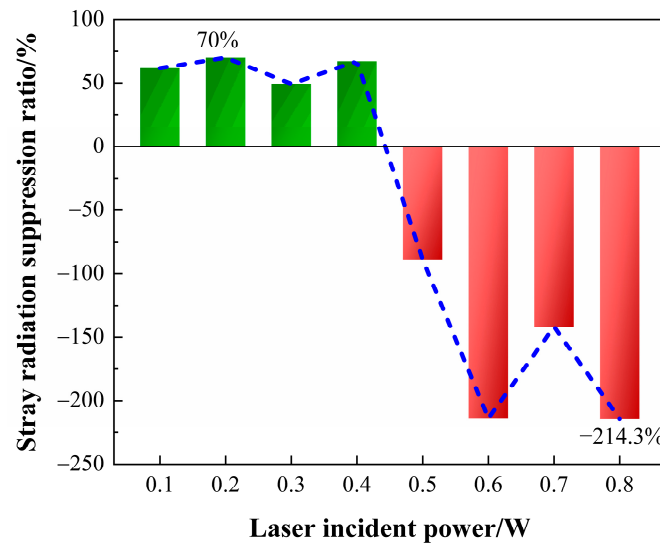


Figure 10. Variation of stray radiation suppression ratio with laser incident power ( $\alpha = 50^\circ$ ).

From Figure 10, it can be seen that, when the laser incident power was no more than 0.4 W, the ceramic coating had the ability to weaken the stray radiation. In this case, the stray radiation intensity was reduced by 70% compared with the case without coating. When the incident laser power exceeded 0.4 W, the ceramic coating could no longer absorb more stray radiation due to the absorption saturation effect. Increasing the ceramic coating could increase the stray radiation; hence, the relative stray radiation suppression ratio  $R_{rel}$  decreased. When the laser power reached 0.8 W, the relative stray radiation suppression ratio  $R_{rel}$  of the ceramic coating was the lowest at  $-214.3\%$ .

### 5.2. Effects of Incident Angle on Stray Radiation

When the incident laser power was unchanged, the most obvious factor affecting the stray radiation intensity in the infrared opto-mechanical system was the laser incident angle. This is because different laser incident angles determine the radiation energy flux into the infrared imaging system, under the same laser power condition. Under the condition of an incident laser power of 0.4 W, the variation of stray radiation intensity in the infrared imaging opto-mechanical system with the laser incident angle was experimentally measured. The stray light distribution image obtained in the experiment is shown in Figure 11. It can be seen that the stray radiation in the infrared opto-mechanical system with ceramic coating was obviously weaker than that without ceramic coating. It is not difficult to conclude that the stray light distribution in the infrared imaging system showed a decreasing trend, indicating that, with the increase in laser incident angle, the laser radiation flux into the infrared imaging system was gradually reduced, and the stray radiation into the system after multiple scattering to the detector image plane was also reduced.

This could also be seen from the variation of the relative intensity of stray radiation with the laser incident angle, as shown in Figure 12. It can be clearly seen that the relative intensity of stray radiation without ceramic coating was generally higher than that with ceramic coating. At the same time, the stray radiation intensity first decreased and then tended to be stable with the increase in laser incident angle. The results show that the stray radiation intensity entering into the infrared opto-mechanical system strongly depended on the change in laser incident angle. When the laser incident angle gradually increased from  $0^\circ$  to  $50^\circ$ , the total stray radiation in the system decreased rapidly. Then, the stray radiation tended to be stable with the further increase in laser incidence angle. The experimental results show that, for the two cases with and without ceramic coating, the stray radiation

intensity formed at the laser incident angle of 50° was the smallest, which was 78.6% and 70.3% lower than that at the laser incident angle of 10°.

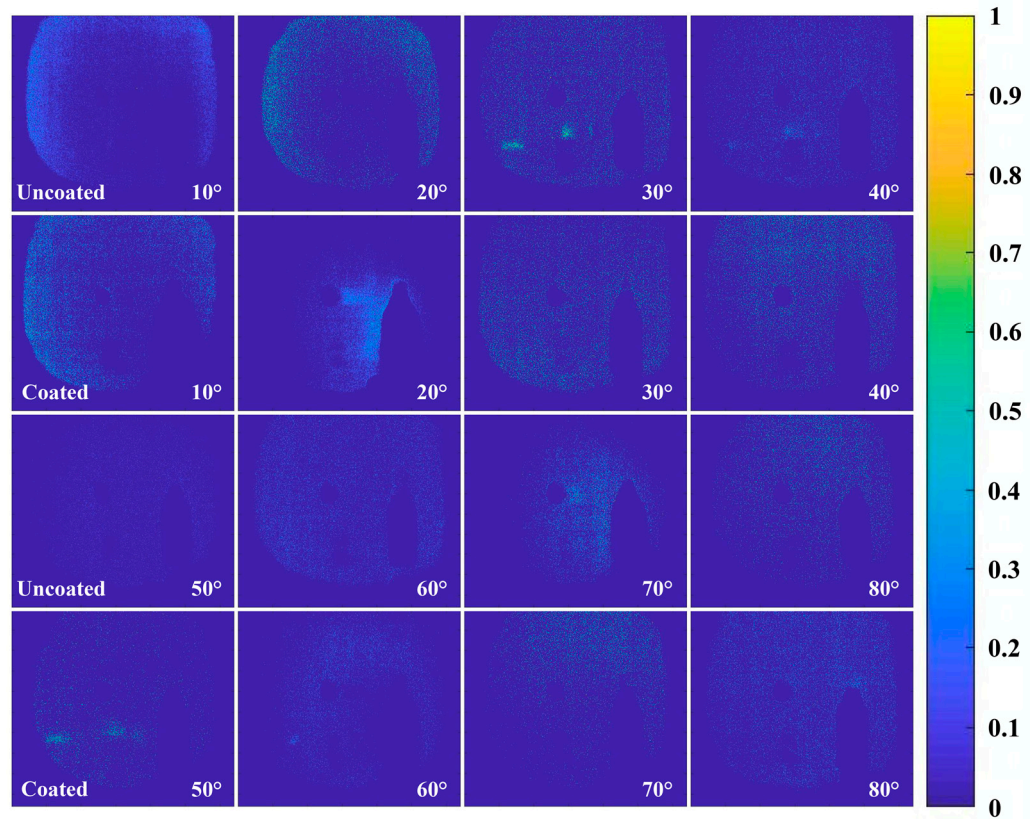


**Figure 11.** Variation of stray light distribution with laser incident angle in optical mechanical system (laser incident power = 0.4 W).

Similarly, by using the definition of average stray radiation suppression ratio  $R_{rel}$  in Equation (12), the variation of  $R_{rel}$  with laser incident angle was obtained under the condition of a laser incident power of 0.4 W, as shown in Figure 13. It can be seen that the average stray radiation suppression ratio  $R_{rel}$  increased first and then decreased rapidly with the increase in laser incident angle. When the laser incident angle reached 50°, the average stray radiation suppression ratio reached the maximum, which was 64.7%. Then, when the laser incidence angle dropped to 80°, the average stray radiation suppression ratio reached the minimum, which was 15.8%.

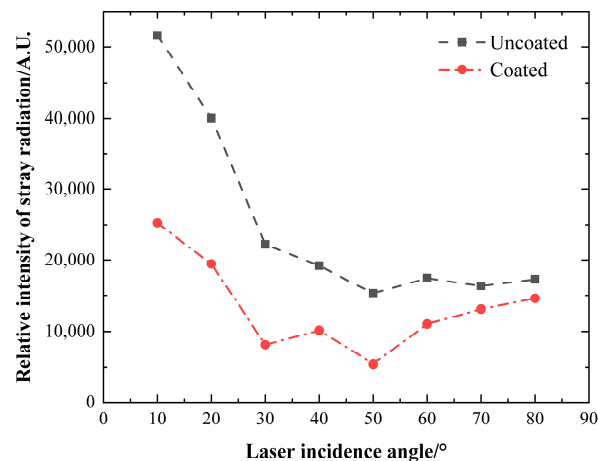


**Figure 12.** Variation of average stray radiation intensity with laser incident angle (laser incident power = 0.4 W).

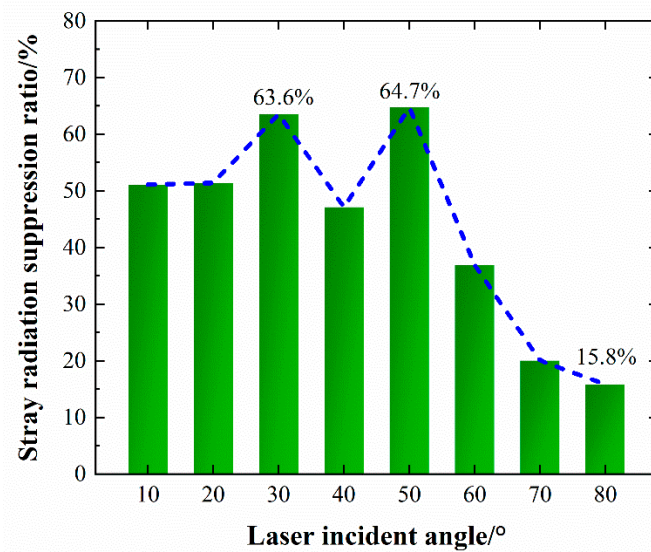


**Figure 13.** Variation of stray radiation suppression ratio with laser incident angle (laser incident power = 0.4 W).

## 6. Conclusions

In conclusion, in order to address the vulnerability of the infrared imaging system to stray radiation caused by an external laser, a novel infrared imaging system with a broadband and high-absorptivity ceramic coating was proposed and developed to suppress the internal stray radiation of the system, which is helpful for enhancing the imaging quality of the detection image in an external laser radiation environment. Firstly, the preparation method and properties of the ceramic coating based on LPPEO technology were studied. Then, a long-wave infrared imaging system with a high-absorption ceramic coating was designed and developed. According to the above results, the suppression ability of the high absorption ceramic coating on the stray radiation in the system was verified for the first time. Lastly, the effects of laser incident power and laser incident angle on the stray radiation were studied. The results are summarized as follows:

- (1) The surface of the high-absorption ceramic coating was characterized by a dense porous structure. It was able to achieve absorption in a wide range of infrared wave band (the average absorptivity of ceramic coating is 95.4% in the range of 0.2–16  $\mu\text{m}$ ) due to the absorption of a large number of micro-pores on the surface of the coating for the radiation from different wave bands. The experimental results showed that there was a saturation upper limit for the absorption capacity of the coating to stray radiation. Under the condition of a laser incident angle of 50°, the saturation absorption laser power threshold of ceramic coating was 0.4 W.
- (2) A novel ceramic coating with a broad absorption band and high absorption was developed, which could obviously suppress the stray radiation in the opto-mechanical system of infrared imaging caused by laser. When the incident laser angle was 50° and the incident laser power was no more than 0.4 W, the ceramic coating could obviously suppress the stray radiation. Then, the stray radiation intensity in the system showed an obvious upward trend with the increase in laser power. At this stage, the ceramic coating mainly played the role of enhancing the stray radiation. The calculation of the average suppression ratio for stray radiation showed that adding a ceramic coating would decrease the stray radiation intensity in the system by 70% compared with that without coating, under the condition of a laser power of 0.2 W. When the laser power was 0.8 W, the average stray radiation ratio of the ceramic coating was lowest at −214.3%.
- (3) When the incident laser power was unchanged, the stray radiation intensity in the infrared opto-mechanical system strongly depended on the change in incident laser

angle. The average stray radiation suppression ratio increased first and then decreased rapidly with the increase in laser incidence angle, under the condition of a laser power of 0.4 W. When the laser incident angle reached 50°, the average stray radiation suppression ratio reached the maximum of 64.7%; when the laser incident angle dropped to 80°, the average stray radiation ratio reached the minimum of 15.8%.

**Author Contributions:** Conceptualization, J.Z. and Z.Y.; methodology, Z.Y., X.G., and S.L.; software, Z.Y. and H.H.; validation, Y.Z. and K.L.; formal analysis, Z.Y. and J.Z.; investigation, Z.Y., J.Z., and K.L.; data curation, X.G.; writing—original draft preparation, Z.Y.; writing—review and editing, J.Z. and Z.Y. supervision, X.G. and K.L.; project administration, J.Z. and Z.Y. All authors have read and agreed to the published version of the manuscript.

**Funding:** This research was funded by the National Key Research and Development Program of China (No. 2017YFB1105000), the National Natural Science Foundation of China (No. 61905053) and a Postdoctoral Fellowship in Heilongjiang Province (No. LBH-Z17092).

**Acknowledgments:** The author would like to thank J.Z., Y.Z., X.G., S.L., H.H., and K.L. for providing many valuable insights and substantial help.

**Conflicts of Interest:** The authors declare no conflict of interest.

## References

1. Smith, C.R.; Grasso, R.; Pledger, J.; Murarka, N. Trends in electro-optical electronic warfare. *Proc. SPIE* **2012**, *8543*, 85430201–85430217.
2. William, C. Requirements for laser countermeasures against imaging seekers. *Proc. SPIE* **2014**, *9251*, 92510301–92510310.
3. Fan, J.X.; Li, L.; Li, W.J. Development of direct infrared countermeasure system and technology. *Infrared Laser Eng.* **2015**, *44*, 789–794.
4. Niu, Y.X.; Zhang, P.; Yao, J.Q.; Duan, X.F.; Wang, Y.Y.; Guo, L. Investigation of laser disturbance and damage to satellite-borne photoelectric detecting system. *Acta Photon. Sin.* **2004**, *33*, 793–796.
5. Li, Y.; Wang, R.Z.; Tittel, F.K.; Ma, Y.F. Sensitive methane detection based on quartz-enhanced photoacoustic spectroscopy with a high-power diode laser and wavelet filtering. *Opt. Lasers Eng.* **2020**, *132*, 106155. [[CrossRef](#)]
6. Pravdivtsev, A.V.; Akram, M.N. Simulation and assessment of stray light effects in infrared cameras using non-sequential ray tracing. *Infrared Phys. Technol.* **2013**, *60*, 306–311. [[CrossRef](#)]
7. Yang, Z.H.; Ma, Y.H.; Guo, J.G.; Jiang, W.W.; Geng, A.H. Analysis and correction of stray thermal radiation in infrared optical systems including an experimental case study. *Appl. Opt.* **2019**, *58*, 3582–3588. [[CrossRef](#)]
8. Wang, G.; Xing, F.; Wei, M.S.; You, Z. Rapid optimization method of the strong stray light elimination for extremely weak light signal detection. *Opt. Express* **2017**, *25*, 26175–26185. [[CrossRef](#)]
9. Sun, C.; Wang, Z.Y.; Cheng, X.H.; Xia, X.L. Simulation and evaluation of stray radiation from optical window effects on infrared detection system. *Infrared Phys. Technol.* **2018**, *94*, 200–206. [[CrossRef](#)]
10. Zhu, Y.; Zhang, X.; Liu, T.; Wu, Y.X.; Shi, G.W.; Wang, L.J. Internal and external stray radiation suppression for LWIR catadioptric telescope using non-sequential ray tracing. *Infrared Phys. Technol.* **2015**, *71*, 163–170. [[CrossRef](#)]
11. Wang, Y.; Shen, Y.Z.; Chen, J.L.; Xu, L.; Mo, D.F.; Liu, D.F. Research of suppressing stray light of cold shield with different black coating. *Proc. SPIE* **2019**, *10841*, 108411701–108411718.
12. He, S.F.; Wang, Y.F.; Dai, C.H.; Liu, J.Y.; Feng, G.J. Analysis and suppression of stray radiation in infrared spectral radiation measurement. *Proc. SPIE* **2019**, *11337*, 11337041–11337047.
13. Reininger, F.M. Stray light performance optimization through system design. *Proc. SPIE* **1994**, *2260*, 17–28.
14. Cranmer, S.R.; Gardner, L.D.; Kohl, J.L. A model for the stray-light contamination of the UVCS instrument on SOHO. *Sol. Phys.* **2010**, *263*, 275–291. [[CrossRef](#)]
15. Buisset, C.; Prasit, A.; Leckngam, A.; Lepine, T.; Poshyajinda, S.; Soonthornthum, B.; Irawati, P.; Richichi, A.; Sawangwit, U.; Dhillon, V.; et al. Progress on the prevention of stray light and diffraction effects on the Thai National Telescope. *Proc. SPIE* **2015**, *9626*, 96262E.
16. Luo, C.J.; Jiao, T.; Gu, J.W.; Tang, Y.S.; Kong, J. Graphene shield by SIBCN ceramic: A promising high-temperature electromagnetic wave-absorbing material with oxidation resistance. *Appl. Mater. Interfaces* **2018**, *10*, 39307–39318. [[CrossRef](#)]
17. Bian, D.; Guo, Y.X.; Zhao, Y.W. Influence of zinc oxide on corrosion resistance of alumina based chemically bonded ceramic coatings. *J. Appl. Chem.* **2016**, *89*, 2091–2094. [[CrossRef](#)]
18. Hlincik, T.; Berka, J.; Kutzendorfer, J.; Hamacek, J.; Sajdl, P. The effect of long-term exposure to high temperature atmosphere on the mechanical properties of Al<sub>2</sub>O<sub>3</sub>-based ceramic materials. *Ceram. Silik.* **2020**, *64*, 35–39. [[CrossRef](#)]
19. Li, W.Z.; Kong, J.; Wu, T.T.; Gao, L.H.; Ma, Z.; Liu, Y.B.; Wang, F.C.; Wei, C.H.; Wang, L.J. Characterization, optical properties and laser ablation behavior of epoxy resin coatings reinforced with high reflectivity ceramic particles. *Mater. Res. Express.* **2018**, *5*, 046202. [[CrossRef](#)]

20. Ji, M.M.; Zhu, S.Z.; Ma, Z.; Li, H.Z. Effects of adhesive modulus and curing conditions on curing behavior of silicate based ceramic coatings on carbon fiber reinforced resin matrix composites. *Ceram. Int.* **2021**, *47*, 11089–11096. [[CrossRef](#)]
21. Yan, D.R.; He, J.N.; Li, X.Z.; Dong, Y.C.; Liu, Y.; Zhang, J.X. Corrosion behavior in boiling dilute HCl solution of different ceramic coatings fabricated by plasma spraying. *J. Therm. Spray Technol.* **2004**, *13*, 503–507. [[CrossRef](#)]
22. Yao, Z.P.; Jiang, Y.L.; Jiang, Z.H.; Wang, F.P.; Wu, Z.D. Preparation and structure of ceramic coatings containing zirconium oxide on Ti alloy by plasma electrolytic oxidation. *J. Mater. Process. Technol.* **2008**, *205*, 303–307. [[CrossRef](#)]
23. Gu, W.C.; Shen, D.J.; Wang, Y.L.; Chen, G.L.; Feng, W.R.; Zhang, G.L.; Liu, C.Z.; Yang, S.Z. Preparation of Al<sub>2</sub>O<sub>3</sub> ceramic coating by electrolytic plasma processing and its properties. *Acta Phys. Sin.* **2005**, *54*, 3263–3267.
24. Chen, Z.; Trice, R.W.; Besser, M.; Yang, X.Y.; Sordelet, D. Air-plasma spraying colloidal solutions of nanosized ceramic powders. *J. Mater. Sci.* **2004**, *39*, 4171–4178. [[CrossRef](#)]
25. Dubourg, L.; Lima, R.S.; Moreau, C. Properties of alumina-titania coatings prepared by laser-assisted air plasma spraying. *Surf. Coat. Technol.* **2007**, *201*, 6278–6284. [[CrossRef](#)]
26. Hu, L.Y.; Song, X.F.; Jin, D.L.; Xing, C.; Shan, X.; Zhao, X.F.; Guo, F.W.; Xiao, P. A robust quasi-superhydrophobic ceria coating prepared using air-plasma spraying. *J. Am. Ceram. Soc.* **2019**, *102*, 1386–1393. [[CrossRef](#)]
27. Deng, W.; Hou, G.L.; Li, S.J.; Han, J.S.; Zhao, X.Q.; Liu, X.; An, Y.L.; Zhou, H.D.; Chen, J.M. A new methodology to prepare ceramic-organic composite coatings with good cavitation erosion resistance. *Ultrason. Sonochem.* **2018**, *44*, 115–119. [[CrossRef](#)]
28. Lu, J.P.; He, X.; Li, H.X.; Song, R.G. Microstructure and corrosion resistance of PEO coatings formed on KBM10 mg alloy pretreated with Nd(NO<sub>3</sub>)<sub>3</sub>. *Materials* **2018**, *11*, 1062. [[CrossRef](#)]
29. Wang, Y.L.; Wang, M.; Zhou, M.; Li, B.J.; Amoako, G.; Jiang, Z.H. Microstructure characterisation of alumina coating on steel by PEO. *Surf. Eng.* **2013**, *29*, 271–275. [[CrossRef](#)]
30. Xu, Y.J.; Yao, Z.P.; Jia, F.Z.; Wang, Y.L.; Jiang, Z.H.; Bu, H.T. Preparation of PEO ceramic coating on Ti alloy and its high temperature oxidation resistance. *Curr. Appl. Phys.* **2010**, *10*, 698–702. [[CrossRef](#)]
31. Molaei, M.; Nouri, M.; Babaei, K.; Fattah-Alhosseini, A. Improving surface features of PEO coatings on titanium and titanium alloys with zirconia particles: A review. *Surf. Interfaces* **2021**, *22*, 100888. [[CrossRef](#)]
32. Darband, G.B.; Aliofkhaezrai, M.; Hamghalam, P.; Valizade, N. Plasma electrolytic oxidation of magnesium and its alloys: Mechanism, properties and applications. *J. Magnes. Alloy.* **2017**, *5*, 74–132. [[CrossRef](#)]
33. Yerokhin, A.L.; Nie, X.; Leyland, A.; Matthews, A.; Dowe, S.J. Plasma electrolysis for surface engineering. *Surf. Coat. Technol.* **1999**, *122*, 73–93. [[CrossRef](#)]
34. Attarzadeh, N.; Molaei, M.; Babaei, K.; Fattah-alhosseini, A. New promising ceramic coatings for corrosion and wear protection of steels: A review. *Surf. Interfaces* **2021**, *23*, 100997. [[CrossRef](#)]
35. Walsh, F.C.; Low, C.T.J.; Wood, R.J.K.; Stevens, K.T.; Archer, J.; Poeton, A.R.; Ryder, A. Plasma electrolytic oxidation (PEO) for production of anodised coatings on lightweight metal (Al, Mg, Ti) alloys. *Trans. Inst. Metal Finish.* **2009**, *87*, 122–135. [[CrossRef](#)]
36. Li, X.; Yao, Z.P.; Li, X.J.; Xu, H.; Xia, Q.X.; Chen, C.J.; Jiang, Z.H. Application of Micro-arc Oxidation Technology in Thermal Control Coating. *Surf. Technol.* **2019**, *48*, 24–36+60.
37. Yao, Z.P.; Li, X.J.; Wei, H.; Xia, Q.X.; Wang, Y.; Li, D.Q.; Jiang, Z.H. Black ceramic coatings on Ti alloy with enhanced high absorptivity and high emissivity by plasma electrolytic oxidation. *Int. J. Appl. Ceram. Technol.* **2019**, *16*, 994–1003. [[CrossRef](#)]
38. Kim, D.; Sung, D.; Lee, J.; Kim, Y.; Chung, W. Composite plasma electrolytic oxidation to improve the thermal radiation performance and corrosion resistance on an Al substrate. *Appl. Surf. Sci.* **2015**, *357*, 1396–1402. [[CrossRef](#)]